Article

Not peer-reviewed version

Sodium Alginate/MXene Based Flexible Humidity Sensors with High-Humid Durability and Application Potentials in Breath Monitoring and Non-Contact Human-Machine Interface

Huizhen Chen , Xiaodong Huang , Yikai Yang , Yang Li *

Posted Date: 27 September 2024

doi: 10.20944/preprints202409.2110.v1

Keywords: Flexible humidity sensor; Sodium alginate; MXene; High-humid durability; Breath monitoring; Non-contact human-machine interface

Article

Sodium Alginate/MXene Based Flexible Humidity Sensors with High-Humid Durability and Application Potentials in Breath Monitoring and Non-Contact Human-Machine Interface

Huizhen Chen, Xiaodong Huang, Yikai Yang and Yang Li *

MOE Key Laboratory of Macromolecular Synthesis and Functionalization, Department of Polymer Science and Engineering, Zhejiang University, Hangzhou 310027, China

* Correspondence: liyang@zju.edu.cn; Tel.: +86-571-87952444.

Abstract: Flexible humidity sensors (FHS) with fast response and durability to high-humidity environment are highly desirable for practical applications. Herein, an FHS based on crosslinked sodium alginate (SA) and MXene was fabricated, which exhibited high sensitivity (impedance varied from 10^7 to 10^5 Ω between 10% and 90% RH), good selectivity, prompt response (response/recover time of 4 s/11 s), high sensing linearity (R^2 = 0.992) on a semi-logarithmic scale, relatively small hysteresis (~5% RH), good repeatability, and good resistance to high humid environment (negligible change in sensing properties after placed in 98% RH over 24 h). It is proposed that the formation of crosslinking structure of SA and introduction of MXene with good conductivity and high specific surface area contributed to the high performance of the composite FHS. Moreover, the FHS could promptly differentiate respiration status, recognize speech and measure fingertip movement, indicating potentials in breath monitoring and non-contact human-machine interactions. This work provides guidance for developing advanced flexible sensors with wide application scope in wearable electronics.

Keywords: Flexible humidity sensor; Sodium alginate; MXene; High-humid durability; Breath monitoring; Non-contact human-machine interface

1. Introduction

In recent years, flexible humidity sensors (FHS) have received considerable attention in respiratory monitoring [1–5], speech recognition [6–8] and non-contact human-machine interface (HMI) [9–14] and demonstrated great potentials for use in wearable electronics. In practical applications, the humidity sensors usually have to work in high-humid environment. For instance, when used for real-time monitoring of breath, the humidity sensors inevitably contact exhaled gas with high humidity (relative humidity (RH) of ~90%), and thus should be resistant to humid environment. Moreover, the humidity sensors should possess fast response in order to keep up with the high frequency of breath in certain scenario (for example, fast breath after exercises). Furthermore, non-contact HMI also relies on the ability of the FHS to promptly respond to humidity change of the micro-environment induced by fingertip movement [15]. In consequence, it is necessary to develop FHS with good durability to humid environment and fast response to satisfy the requirements for applications.

It is well-known that the sensing performance of FHS is highly dependent on the humidity sensing materials. Polyelectrolytes are typical humidity sensing materials with features of high sensitivity, easy preparation, etc. However, such materials generally show the defects of slow response/recovery speed. To tackle the problems, blending with nanostructured materials to improve specific surface area of sensitive film offers an effective solution. For instance, Yuan and coworkers [16] used two-dimensional (2D) nanomaterial of graphene oxide (GO) to form a composite with

 doi:10.20944/preprints202409.2110.v

polyethyleneimine. As-prepared sensitive film showed rough and wrinkle structure, presenting large surface area and fast response (response and recovery time of 5 s and 8 s, respectively). Wu et al. [17] prepared a humidity sensor based on UIO-66 derived polyelectrolyte. Benefited from specific pore size of the framework, the as-prepared sensor showed small hysteresis (~1.2% RH) and short response/recovery time of 3.1 s/1.5 s.

Furthermore, the polyelectrolytes used as humidity sensing materials are mainly water-soluble which bestows them good processability to facilitate the sensor fabrication. However, such linear polymers could not withstand high humidity environment, and the corresponding humidity sensors would exhibit deteriorated sensing performance in humid environment since the polyelectrolytes would get dissolved and lost in highly humid environment [18]. To endow the FHS with good durability against high-humid environment, the introduction of crosslinking structure in the polyelectrolyte sensing films could be a feasible approach. Dai et al. [19] used gaseous 1,4-dichlorobutane to crosslink poly(4-vinylpyridine) and the resulting humidity sensor presented good stability and did not show any performance degradation when exposed to high humidity (95% RH) for more than 30 min.

Herein, a FHS was fabricated based on a nanocomposite of crosslinked sodium alginate (SA) and MXene which is a well-known 2D nanomaterial with high conductivity and large specific surface area. Specifically, polyimide (PI) film was employed as the flexible substrate of the sensor, on which interdigitated electrodes (IDEs) were constructed by using the method of laser direct writing (LDW) to convert PI to conductive graphene. The composite sensing material of SA/MXene loaded on the surface of PI film was further treated with $CaCl_2$ to introduce a cross-linking structure to improve the durability to high humidity. The as-prepared FHS exhibited good sensitivity, fast response (4 s/11 s), high selectivity and good sensing repeatability. In particular, the FHS showed little change in the sensing performance even after placed in humid environment for up to 24 hours, revealing high resistance to high humidity. Moreover, it could successfully realize respiratory monitoring, speech recognition and detection of slight movement of fingertip in a non-contact way. The work offered an effective solution for the development of advanced flexible nanosensors with fast response and good durability towards humid environment with wide application scope.

2. Experimental

2.1. Materials and Reagents

Ti_3AlC_2 (400 mesh) was provided by Shandong Xiyan New Material Science and Technology Co., Ltd. Hydrogen fluoride (HF), SA, sodium hydroxide (NaOH), lithium chloride (LiCl), magnesium chloride hexahydrate ($MgCl_2{\cdot}6H_2O$), sodium bromide (NaBr), sodium chloride (NaCl) and potassium sulfate (K_2SO_4) were purchased form Sinopharm Chemical Reagent Co., Ltd. Calcium chloride ($CaCl_2$) was obtained from Quzhou Juhua Reagent Co., Ltd. PI film was supplied by Shenzhen Yingshida Plastic Materials Co., Ltd.

2.2. Preparation of Crosslinked SA (c-SA)/MXene FHS

The preparation process of the composite FHS is shown in Figure 1. First, MXene was prepared by etching Ti_3AlC_2 (MAX phase) with HF according to a method described in previous research [20]. Typically, 1 g Ti_3AlC_2 powder and 15 mL HF were added into a 50 mL Teflon reactor and magnetically stirred for 24 h. The resultant was centrifuged at 5000 r/min for 5 min and the isolated solid product was redispersed in water. The operation was repeated several times until the pH of the supernatant was ~ 6. The isolated solid product was freeze-dried for 4 h using a lyophilizer (FD-1A-50, Beijing Boyikang Experimental Instrument Co., Ltd., China) to obtain MXene powder.

 doi:10.20944/preprints202409.2110.v

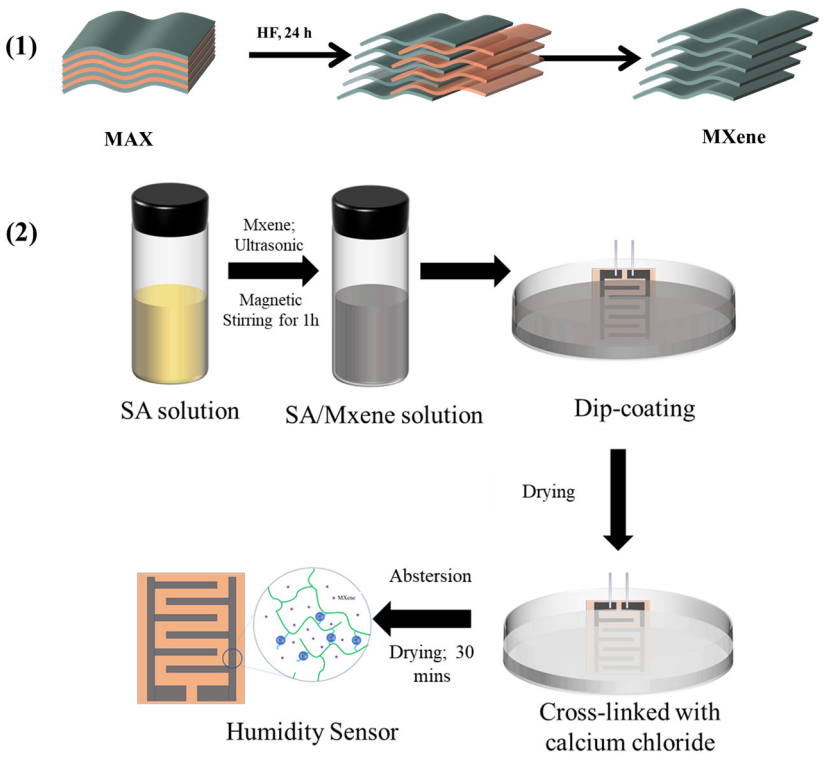

Figure 1. Preparation of c-SA/MXene FHS.

PI film was hydrophilically modified by soaking in NaOH solution (1 mol/L) for 30 min, washed with deionized water thoroughly, and dried at 80°C for 30 min. IDEs were fabricated on the modified PI film by a CO_2 laser engraver to convert PI into graphene (scanning speed: 100 mm/s, power: 9.6 W, line spacing: 1 mm, Tianjin Jiayin Nanotechnology Co., Ltd., China). Detailed parameters of the IDEs are shown in Figure 2.

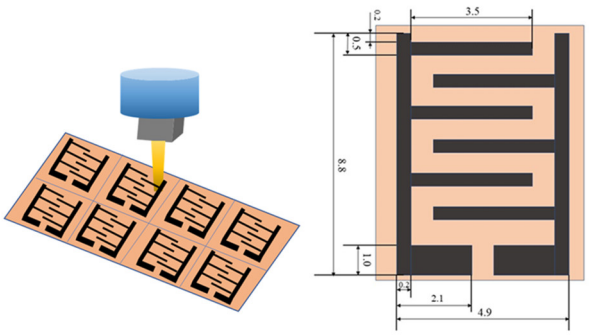

Figure 2. Preparation of IDEs and its detailed parameters.

As shown in Figure 1 (2), various amount of MXene was added into aqueous solution of SA (4 mg/mL) and magnetically stirred for 1 h to prepare uniform dispersion of SA /MXene. The PI films with IDEs were immersed in the dispersion of SA /MXene for 1 min, and then dried at 50°C for 30 min. As-prepared sample was named as SA/MXeneα, where α is the concentration of MXene in the dispersion in mg/mL. Subsequently, the sample was immersed in $CaCl_2$ solution (5 wt%) for the crosslinking of SA, then washed with deionized water and dried at 50°C for 30 min. The resulting FHS was named as c-SA/MXeneα-β, where β is crosslinking time in min.

2.3. Characterizations

 doi:10.20944/preprints202409.2110.v

Morphologies of Ti_3AlC_2, MXene, FHS of SA/MXeneα and c-SA/MXeneα-β were analyzed by field emission scanning election microscopy (FE-SEM, Hitachi SU-8010). Fourier transform infrared (FTIR) spectra (KBr pellets) and attenuated total reflection infrared Fourier transform infrared (ATR-FTIR) spectra were obtained on a Dell TENROS II. Raman spectrum was collected on a Raman spectrophotometer (INVIA-REFLEX) with a He-Ne laser (λ = 532 nm).

2.4. Measurements of Humidity Sensing Properties

Real-time humidity response of the FHS was measured with a home-made device in a chamber where relative humidity (RH) was controlled by adjusting the mixed ratio of dry and wet gases, and calibrated with a commercial hygrometer (Rotronic, Hygroclip HC2-S3) at room temperature (~25°C). The test voltage was AC 1 V with frequency of 1 kHz. The diagram of humidity testing device is shown in Figure 3.

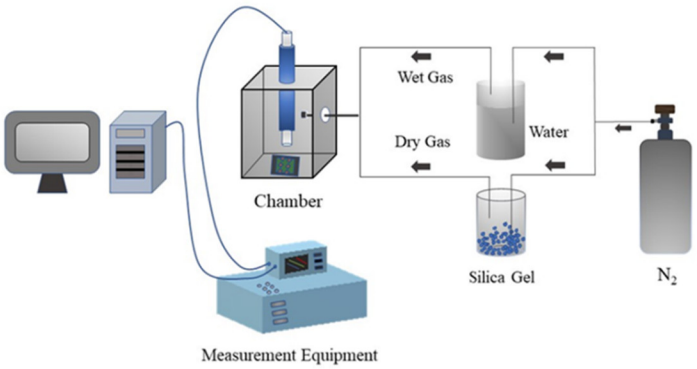

Figure 3. Schematic diagram of humidity testing device.

The response/recovery time ($t_{90\%}$) of the sensor is defined as the time required for the impedance of the sensor to reach 90% of the total change.

To study the stability of the FHS in humid environment, the sensor was placed under 98% RH for 9 h, and its impedance was recorded online using an intelligent LCR meter (4092C, Shenzhen Yisheng Victory Technology Co., Ltd.). Furthermore, the FHS was put under 98% RH for 24 h and then the sensing performance of the FHS before and after treatment in the high-humid environment was tested. The ambient humidity was 70% RH (±1%RH) and the temperature was 22 °C (±0.5 °C). The test voltage was AC 1 V and the frequency was 1 kHz.

To test the effect of organic vapors on impedance response of the FHS, the impedance of c-SA/MXene1-30 FHS before and after exposure to organic vapors (ethanol, ether, methanol, acetone, and n-hexane) was measured at 74% RH and 27 °C. Specifically, calculated amount of the liquids of the organic solvents were injected into a vessel fitted with a small electric fan for the volatilization of the liquid to obtain organic vapors of 500 ppm. The gas response S of the FHS is defined as follows:

$$S = \frac{R\text{-}R_0}{R_0} \times 100 \quad (1)$$

where R and R_0 are the impedance before and after exposure to organic vapors for 5 min, respectively.

The repeatability of c-SA/MXene1-30 FHS was examined by recording its impedance in real-time when the sensor was switched between high humid (98% RH) and dry (11% RH) environment at an interval of 30 s for 120 cycles at room temperature (~25°C).

Nyquist plots of the sensor under different humidity levels (11, 33, 59, 75 and 98% RH) were recorded on a ZL5 intelligent LCR meter (Shanghai Haoshun technology Co. Ltd.) at room temperature. Various stable humidity environments were provided by usin saturated salt solutions (LiCl: 11% RH; MgSO4: 33% RH; NaBr: 59% RH; NaCl: 75% RH; K2SO4: 98% RH).

2.5. Application of c-SA/MXene1-30 FHS

 doi:10.20944/preprints202409.2110.v

(1) Real-time respiratory monitoring: The FHS was placed close to the mouth or under the nose of a volunteer, and the real-time impedance of the sensor during the respiration in different modes was recorded using a ZL5 intelligent LCR meter. The ambient humidity was 51% RH (±1% RH) and the temperature was 25 °C (±0.5 °C).

(2) Speech recognition: The FHS was displayed in front of the lip of the volunteer, and real-time impedance of the sensor was recorded with a ZL5 intelligent LCR meter. The volunteer spoke different words such as "pen", "paper" and "potato", and corresponding signal was recorded. The ambient humidity was 75% RH (±1% RH) and the temperature was 25 °C (±0.5 °C).

(3) Non-contact detection of fingertip movement: the impedance change of the FHS was recorded online with a ZL5 intelligent LCR meter when the fingertip of the volunteer cyclically moved between sufficiently far place (distance > 40 cm) and close to the sensor (distances: 8 mm, 3 mm and 1 mm). The ambient humidity was 75% RH (±1% RH) and the temperature was 25 °C (±0.5 °C).

3. Results and Discussion

3.1. Characterization of FHS

In this work, we prepared MXene by etching with HF as shown in Figure 1, and the SEM images of MAX phase and MXene are illustrated in Figure 4 (a) and (b). It is seen that MAX phase comprises uneven and tightly packed blocks. In comparison, the MXene is composed of accordion-like multilayers with layer thickness in the range of nanoscale, which is expected to show high specific surface area and provide more active sites for the adsorption of water molecules. Figure 4 (c-g) present the morphology of FHS with different concentration of MXene. SA alone exhibits smooth surface, while MXene debris are clearly observed on the surface of the composite of SA/MXene. With the increment of the concentration of MXene, the composite exhibits rougher surface with higher density of MXene debris. Furthermore, the composite film shows little change in the morphology after crosslinking of SA with $CaCl_2$ as evidenced by comparison of Figure 4 (f) with (g).

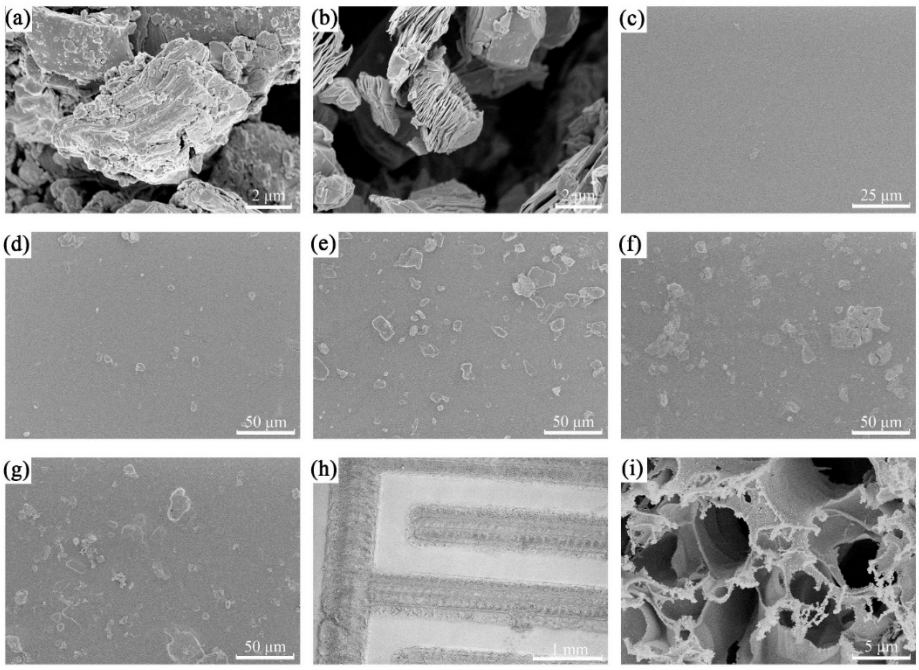

Figure 4. SEM micrographs of (a) MAX phase (Ti_3AlC_2); (b) MXene; (c) SA; (d) SA/MXene0.5; (e) SA/MXene1;(f) SA/MXene2;(g) c-SA/MXene1-30; IDEs at (h) low magnification and (i) high magnification.

Figure 4 (h) and (i) present the SEM images of IDEs constructed on PI film. The boundary of the area treated with LDW and without LDW treatment is clear, indicating high resolution of the

 doi:10.20944/preprints202409.2110.v

patterned structure induced by LDW treatment. At high magnification, IDEs reveal rugged and porous surface, which is attributed to the conversion of PI to the conductive graphene by laser treatment and is in agreement with literature reports [21].

The chemical structure of the samples has been examined by the analysis of FT-IR spectroscopy. In the FT-IR spectrum of MXene (Figure 5 (a)), the absorption peaks at 3435 cm^{-1} and 1625 cm^{-1} are ascribed to hydrogen-bonded -OH or water molecules coordinated on the surface of MXene. Furthermore, the characteristic peak at 1257 cm^{-1} is attributed to the stretching vibration of C-F [22]. The FT-IR characterization indicates the existence of functional groups like -OH and -F attached to the surface of MXene.

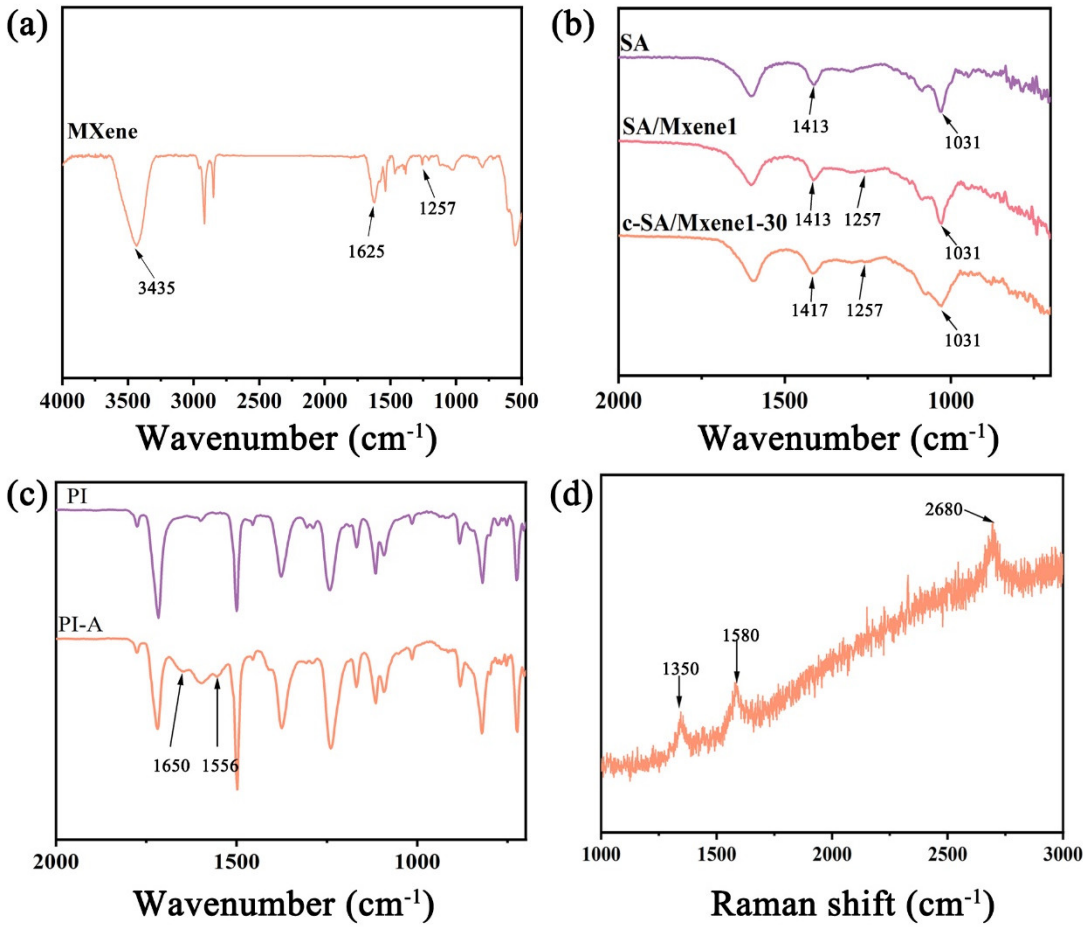

Figure 5. (a) FT-IR spectrum of MXene; ATR-FTIR spectra of (b) SA, SA/MXene1 and c-SA/MXene1-30; (c) PI and PI-A; (d) Raman spectrum of IDEs in PI.

Figure 5 (b) shows the ATR-FTIR spectra of SA, SA/MXene1 and c-SA/MXene1-30. In the spectrum of SA, the absorption peak at 1031 cm-1 represents the symmetric stretching vibration of C-O on C-O-C [23]. The characteristic peak 1413 cm^{-1} is attributed to symmetric stretching of –COO– on the polymer chain [24]. In the spectrum of MXene, the peak at 1257 cm^{-1} is ascribed to C-F in MXene [22]. Both characteristic peaks of MXene and SA are clearly identified in the spectrum of SA/MXene1. In comparison, in the spectrum of c-SA/MXene1-30, the absorption peak corresponding to symmetric stretching of –COO– on SA is shifted from 1413 cm^{-1} to 1417 cm^{-1}, which is attributed to the crosslinked structure between $CaCl_2$ and SA [24]. The above results indicate the successful preparation of SA/MXene and c-SA/MXene.

The ATR-FTIR spectra of PI and PI-A are shown in Figure 5 (c). Compared with PI, in the ATR-FTIR spectrum of PI-A, new absorption peaks appear at 1556 cm^{-1} and 1650 cm^{-1}, which are assigned to the N-H bending vibration peaks and C=O stretching vibration peaks, respectively. The observation of such new functional groups proves the hydrolysis of imide group of PI by the treatment with NaOH [25].

 doi:10.20944/preprints202409.2110.v

Figure 5 (d) shows the Raman spectrum of the IDEs formed by laser treatment in the PI substrate. Three prominent peaks in the spectrum are identified at 1350 cm^{-1}, 1580 cm^{-1} and 2680 cm^{-1}, corresponding to the D band, G band and 2D band of graphene, respectively [26] .The D band is related to the conversion of sp^2 hybridized carbon to sp^3 hybridized carbon, while the G band is related to the vibration of sp^2 hybridized carbon [27]. Obviously, the Raman characterization reveals that the LDW-induced IDEs are composed of conductive graphene.

3.2. Humidity Sensing Properties of FHS

Figure 6 (a) presents the humidity sensing curves of SA/MXene FHS with different concentration of MXene. The impedance of the FHS based on SA varies from ~10^6 Ω to 10^7 Ω within the range of 90% RH to 10% RH, showing relatively low sensitivity and high impedance even under humid environment. It is well-known that SA is a kind of natural polyelectrolyte with a large number of hydrophilic functional groups. With the increase of RH, more water molecules are absorbed in SA film, which are decomposed to produce protons and also promote the dissociation of Na^+ in SA to improve ion conductivity, leading to the decrement of impedance. However, the sensitivity of SA is limited, which can be further improved by compositing with nanomaterials with large specific area and high conductivity. Herein, MXene was introduced into the sensitive film, and the resulting sensing curves are shown in Figure 6 (a). The FHS based on the composite of SA/MXene exhibited much lower impedance than that bases on SA alone at every RH investigated. which is attributed to excellent conductivity of MXene. Moreover, the composite sensor revealed much higher sensitivity than the sensor of SA. As a typical 2D nanomaterial, MXene possesses large specific area and abundant hydrophilic groups (such as -OH), which could provide sufficient active sites for the adsorption of water molecules and therefore improve the sensitivity of composite film. Specifically, when the concentration of MXene in the composite solution reaches 2 mg/mL, the impedance of corresponding sensor decreased dramatically over the whole tested humidity range. It is proposed that conducting path was well established in the composite film at such a high concentration of highly conductive MXene, leading to greatly improved conductivity of the composite sensor. Therefore, the variation of adsorbed water molecules with the change of RH did not result in much change in the conductivity, and the sensor demonstrated lower sensitivity. In the work, 1 mg/mL of MXene is selected as the optimal formula for the fabrication of the composite FHS.

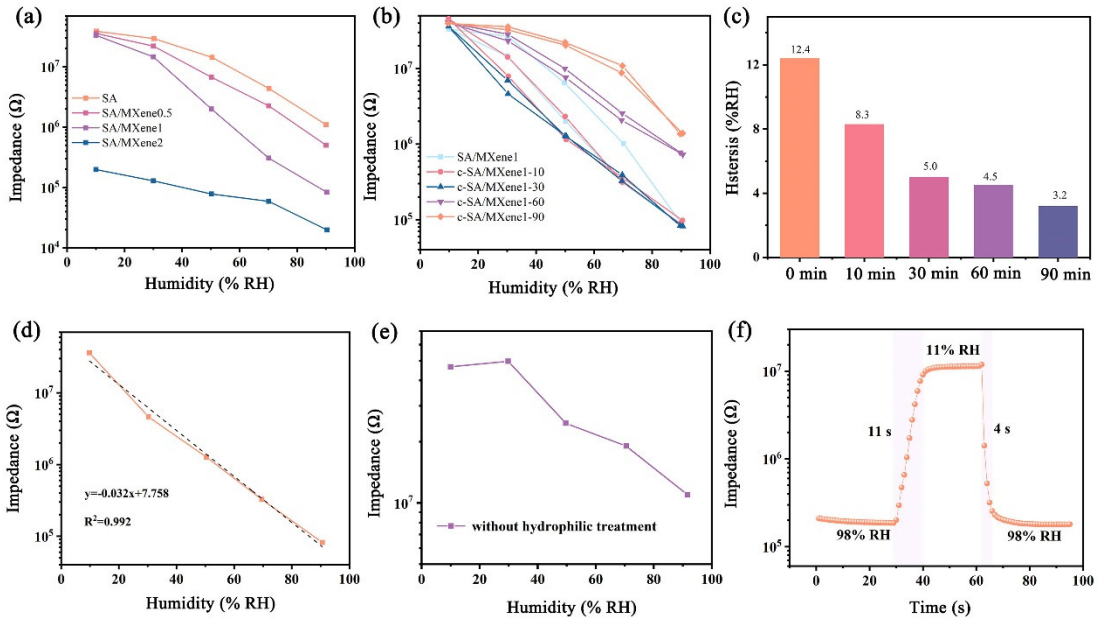

Figure 6. Humidity sensitive curves of FHS prepared with (a) different concentration of MXene; (b) different crosslinking time; (c) hysteresis of FHS with different crosslinking time; (d) humidity sensitive curve; (e) linearity; (f) response and recovery time of c-SA/MXene1-30 FHS.

 doi:10.20944/preprints202409.2110.v

Figure 6 (b) shows the influence of crosslinking time on the humidity sensing properties of c-SA/MXene FHS. The FHS of SA/MXene exhibited quite large hysteresis of ~12.5% RH. In comparison, the FHS based on c-SA/MXene obtained by immersion in $CaCl_2$ solution showed much decreased hysteresis. Specifically, extending the immersion time of FHS in $CaCl_2$ solution leads to smaller hysteresis and higher sensitivity. It has been reported that SA could react with Ca^{2+} to form a stable intermolecular cross-linking network structure [28]. Apparently, such crosslinked structure is helpful to hinder the accumulation of water molecules and avoid the formation of water layer in the sensing film, resulting in smaller hysteresis of the FHS. When the cross-linking time reaches 60 min, the sensor exhibited relatively small hysteresis of ~5.0% RH. Further increasing the immersion time could lead to even smaller hysteresis, but the sensitivity of the FHS is decreased, too. Immersion time of 30 min is thus chosen as optimal formula by considering the sensitivity and hysteresis. The c-SA/MXene1-30 FHS exhibited impedance change of two orders of magnitude and good sensing linearity (R^2 = 0.992, Figure 6 (d)) on a semi-logarithmic scale over a wide range of 11-98%RH. Moreover, it revealed fast response/recover time (4 s/11 s, Figure 6 (f)), which might be ascribed to the high specific surface area of MXene and accelerated desorption of water molecules due to the formation of crosslinked structure.

Additionally, humidity sensing curve of the FHS based on c-SA/MXene1-30 with PI without hydrophilic treatment as the substrate is presented in Figure 6 (e) to explore the effect of surface modification on the humidity response of the FHS. The sensor with unmodified hydrophobic PI as the substrate showed very high impedance of over 10^7 Ohm in the whole tested humidity range (10-90% RH) with slight variation in the impedance. It is proposed that the incompatibility between hydrophobic substrate and hydrophilic sensitive materials hindered the deposition of the sensitive film on the flexible substrate, leading to poor sensitivity of resulting FHS. Apparently, the results revealed the importance of NaOH treatment of PI film for the fabrication of high performance composite FHS.

As discussed before, the stability under humid environment is crucial for the practical applications of FHS. Herein, c-SA/MXene1-30 FHS was placed in 98% RH for over 9 h and the real-time impedance response is illustrated in Figure 7 (a). Clearly, the FHS did not show any degradation in sensing performance during the storage in the highly humid environment. Furthermore, the FHS was placed in a bottle containing water at 40°C for 24 h, and its humidity responses before and after the exposure to the humid environment changed little as shown in Figure 7 (b). The results clearly demonstrated that the FHS exhibited good durability towards humid environment, which might relate to the formation of crosslinking structure of SA in the composite film. Additionally, the responses of c-SA/MXene1-30 FHS to organic gases (methanol, ethanol, ether, acetone and n-hexane) are presented in Figure 7 (c). The FHS exhibited quite small response towards all the tested organic gases, demonstrating excellent selectivity of c-SA/MXene1-30 FHS. Figure 7 (d) displays the real-time responses of c-SA/MXene1-30 FHS during quick switching between high and low humidity environment for 120 cycles at an internal of 30 s. Clearly, the early, middle and late stages of the sensing curves show almost the same impedance values at high and low humidity levels and unchanged shapes, suggesting good sensing repeatability and stability of FHS.

 doi:10.20944/preprints202409.2110.v

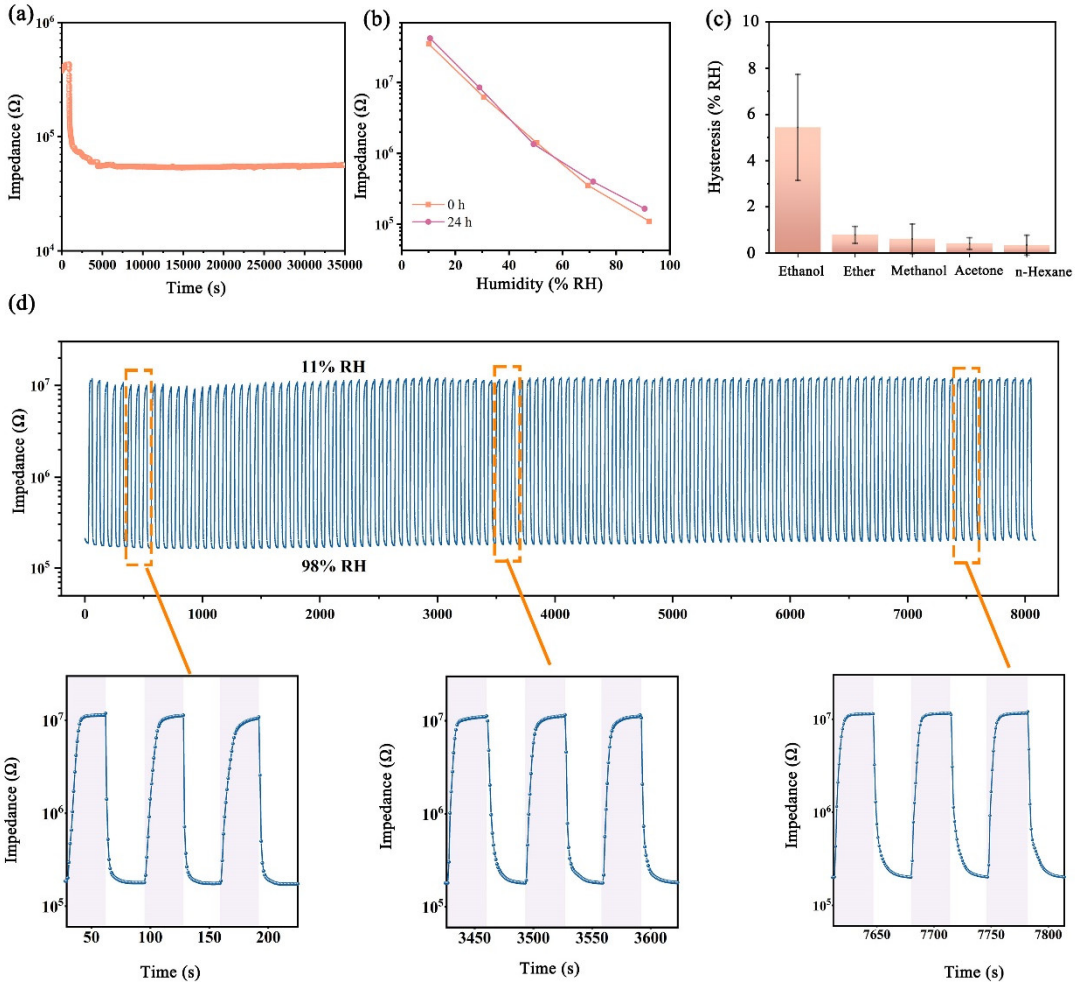

Figure 7. (a) real-time response of c-SA/MXene1-30 FHS displaced in 98% RH for over 9 h; (b) humidity response of c-SA/MXene1-30 FHS when the FHS was placed in 98% RH of 0 h and 24 h; (c) response of c-SA/MXene1-30 FHS when exposed to 500 ppm vapors of different analytes: ethanol, ether, methanol, acetone, n-hexane; (d) response of c-SA/MXene1-30 FHS during cyclic switching between high and low humidity environment.

Nyquist plots of c-SA/MXene1-30 FHS under various humidity environment were measured to explore the humidity sensing mechanism. As shown in Figure 8 (a), when the humidity is below 33% RH, the Nyquist plot of the sensor is composed of a semicircle. In comparison, the Nyquist plots are composed of a semicircle at high frequency and a straight line at low frequency under 59-98% RH. The semicircle represents the membrane impedance of the sensor, while the straight line is ascribed to Warburg impedance of the diffusion process [29]. Under low humidity level, limited water molecules are adsorbed on the humidity sensing film, resulting in poor ion conductivity. Therefore, the Nyquist plots are composed of a semicircle with large radius. With the increase of humidity, more and more water molecules are adsorbed on the humidity sensing film, which are decomposed and also promote the dissociation of ion in the sensing film to result in high ion conductivity and thus much smaller semicircle radius. At high humidity level, a large number of adsorbed water molecules form a continuous water layer on the surface of the sensing film (Figure 8b), significantly enhancing ion conduction and playing a dominant role in the overall conductivity of the sensor.

 doi:10.20944/preprints202409.2110.v

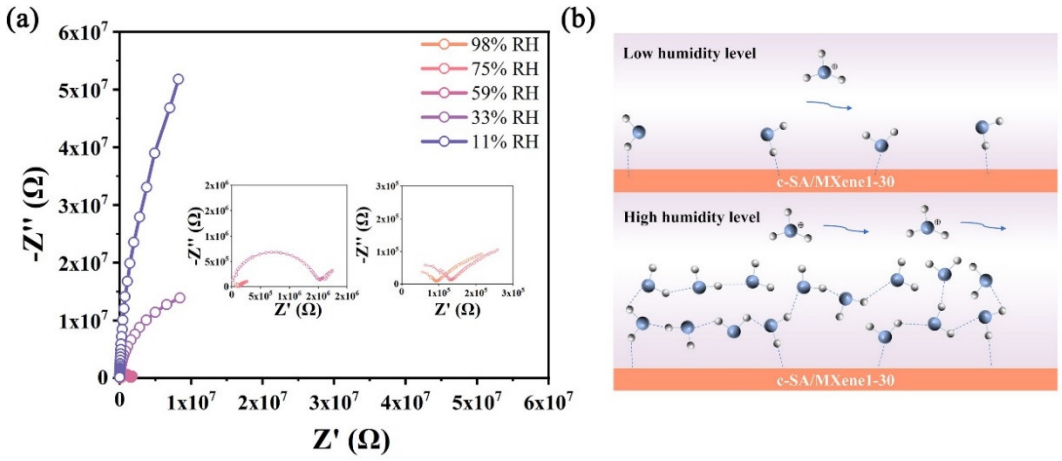

Figure 8. (a) Nyquist plots of c-SA/MXene1-30 FHS under different humidity levels; (b) diagram of proposed sensing mechanism.

3.3. Applications of FHS

The exhaled air of human is highly humid, and could change the humidity in surrounding microenvironment [30]. Therefore, the detection of breath-induced humidity change could be utilized to reflect the respiration status for non-invasive and non-contact early diagnosis [31,32]. Herein, the c-SA/MXene1-30 FHS was assembled in a mask and worn by a volunteer to verify its potentials for respiratory monitoring. The real-time responses of the FHS towards the respiration of the volunteer at different breathing modes are shown in Figure 9 (a-c). It is seen that the response curves exhibit distinct amplitude and frequency towards three different breathing modes. Apparently, the response curves exhibited the largest amplitude and the lowest frequency towards the slow breathing mode, while the sensing curves with the smallest amplitude and the highest frequency indicated fast breathing mode. It is proposed that during the breathing process, exhaled gas carries a large amount of water molecules, which increases the humidity of the air around mouth and leads to the decrease of the impedance of the sensor. By contrast, the water vapor content is lowered during inhalation and the humidity around mouth decreases, resulting in higher impedance for the sensor. In slow breathing rate, the FHS could adsorb/desorb water molecules more efficiently and thus exhibit larger impedance change and greater amplitude in the sensing curve. Obviously, our FHS with fast response could well differentiate the respiratory patterns, revealing potentials in non-contact respiratory motoring.

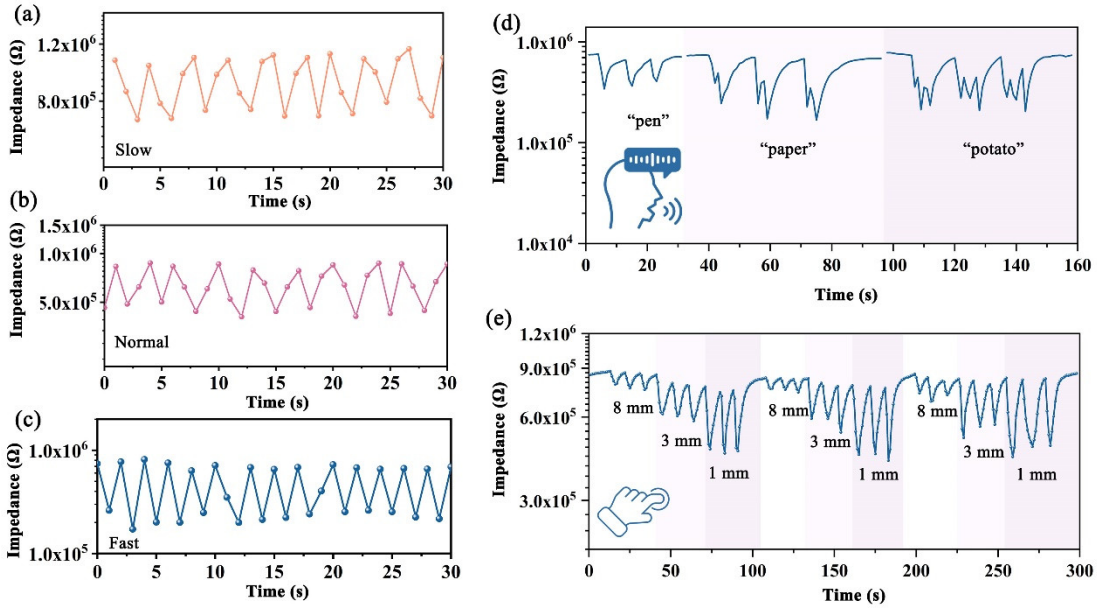

 doi:10.20944/preprints202409.2110.v

Figure 9. Application of c-SA/MXene1-30 FHS: respiration monitoring under different states: (a) slow speed; (b) normal speed; (c) fast speed; (d) speech recognition; (e) real-time impedance response of distance change between the sensor and fingertips.

Similarly, the exhaled airflow during speaking leads to the vibration of the vocal cords to produce sound, which is then modulated into different syllables through the mouth and nose to form specific words. Apparently, the process of speaking is accompanied by humidity change of air around the mouth. Therefore, the detection of the humidity change in the microenvironment could be utilized to distinguish different syllables. In this work, a volunteer said different words (monosyllabic (pen), disyllabic (pencil), and trisyllabic (tomato)) and the real-time response of the c-SA/MXene1-30 FHS assembled around the mouth of the speaker was recorded (Figure 9 (d)). It is clear that the FHS exhibited characteristic and repeatable sensing curves towards various syllables, indicating the potentials of speech recognition by c-SA/MXene1-30 FHS.

There have been a number of reports on the application of humidity sensors in non-contact HMI [33–35]. Herein, the real-time impedance response of c-SA/MXene1-30 FHS was recorded as the fingertip of a volunteer approached the sensor at different distances of 1 mm, 3 mm, and 8 mm, and the results are displayed in Figure 9 (e). It is found that FHS exhibited sensitive, reversible and repeatable responses towards the change of the distance between the sensor and fingertip, proving its capability of detecting the delicate movement of fingertip in a non-contact way. Obviously, the results indicate that the c-SA/MXene1-30 FHS shows potentials for non-contact HMI, which can be used for reducing the risk of virus transmission such as COVID-19 during large-scale infectious disease outbreaks.

4. Conclusions

An FHS was facilely fabricated by depositing the nanocomposite of crosslinked SA and MXene on NaOH modified PI substrate. The composite FHS exhibited fast response and good durability towards highly humid environment due to the introduction of 2D nanomaterials of MXene with high specific surface area and good conductivity and the formation of stable crosslinking structure between SA and Ca^{2+}. Moreover, as-prepared FHS was featured with high sensitivity (impedance change of two orders of magnitude between 10% and 90% RH), good selectivity and sensing repeatability. The high performance FHS demonstrated great potentials for the monitoring of respiration, speech recognition, and non-contact HMI by detecting the delicate movement of fingertip. This work provides a feasible approach for improving the sensing performance of flexible nanosensors by simply modifying the structure and composition of the sensing film to satisfy the requirements for practical applications in wearable electronics.

Author contributions: Conceptualization: H.Z. Chen. and Y. Li; methodology: H. Z. Chen and Y. Li; investigation: H. Z. Chen, X. D. Huang and Y. K. Yang; validation: H. Z. Chen, X. D. Huang and Y. K. Yang; resources: Y. Li; writing—original draft preparation: H. Z. Chen, X. D. Huang and Y. K. Yang; writing—review and editing: H. Z. Chen, X. D. Huang and Y. Li; project administration: Y. Li; funding acquisition: Y. Li. All authors have read and agreed to the published version of the manuscript.

Declaration of Competing Interest: The authors declare no conflict of interest.

Acknowledgments: This work was financially supported by Basic Public Welfare Research Program of Zhejiang Province, China (No. LGG21E030006).

References

1. Yan, S.Z.; Shen, D.D.; Xin, B.J.; Newton, M.A.A.; Wu, Y. Rhombus-patterned flexible self-supported PVDF-based humidity sensor for respiratory monitoring. *Polymer.* **2023,** *282*, 126139. https://doi.org/https://doi.org/10.1016/j.polymer.2023.126139
2. Pan, M.X.; Zhou, J.M.; Weng, S.C.; Wu, X.J. Flexible Chitosan-Based Capacitive Humidity Sensors for Respiratory Monitoring. *Sensors.* **2024,** *24*, 1352. https://doi.org/10.3390/s24051352

3. Chen, X.Y.; Mei, S.X.; Zhao, W.; Zhang, Y.C.; Zhang, X.M.; Cui, Z.; Fu, P.; Pang, X.C.; Liu, M.; Ye, Y. Thermoplastic polyamide elastomer based flexible humidity sensor for breath monitoring. *Mater. Des.* **2023,** *235*, 112438. https://doi.org/https://doi.org/10.1016/j.matdes.2023.112438
4. Wang, Y.K.; Hu, C.; Li, Z.X.; Zhao, Q.L.; Wang, H.Y.; Chen, J.H.; Zheng, D.Z.; Yang, G.Y.; Liu, B. A fast response humidity sensor based on MXene-SWCNTs for the monitoring of respiration. *Sens. Actuators, B.* **2024,** *410*, 135655. https://doi.org/https://doi.org/10.1016/j.snb.2024.135655
5. Zhang, H.W.; Xu, X.; Huang, M.L.; Wang, Y.S.; Xu, Z.Q.; Feng, Z.S.; Zhang, Y.g.; Wang, Y. Interlayer cross-linked MXene enables ultra-stable printed paper-based flexible sensor for real-time humidity monitoring. *Chem. Eng. J.* **2024,** *495*, 153343. https://doi.org/https://doi.org/10.1016/j.cej.2024.153343
6. Tang, C.L.; Wang, H.X.; Dou, Y.H.; Lai, P.G. Meshed, Flexible, and Self-Supported Humidity Sensors by Direct-Writing with Multifunctional Applications. *ACS Omega.* **2024,** *9*, 33261-33269. https://doi.org/10.1021/acsomega.4c05316
7. Xiang, H.C.; Li, Z.J.; Zheng, H.X.; Jiang, X.H.; Wu, H.W.; Zhou, H.W.; Liu, H.B. Disposable, strain-insensitive, and room-temperature-operated flexible humidity and VOC sensor with enhanced sensitivity and selectivity through interface control. *Sens. Actuators, B.* **2024,** *399*, 134831. https://doi.org/https://doi.org/10.1016/j.snb.2023.134831
8. Duan, Z.H.; Jiang, Y.D.; Huang, Q.; Wang, S.; Wang, Y.; Pan, H.; Zhao, Q.N.; Xie, G.Z.; Du, X.S.; Tai, H.L. Paper and carbon ink enabled low-cost, eco-friendly, flexible, multifunctional pressure and humidity sensors. *Smart Mater. Struct.* **2021,** *30*, 055012. https://doi.org/10.1088/1361-665X/abe87d
9. Lu, L.J.; Jiang, C.P.; Hu, G.S.; Liu, J.Q.; Yang, B. Flexible Noncontact Sensing for Human–Machine Interaction. *Adv. Mater.* **2021,** *33*, 2100218. https://doi.org/https://doi.org/10.1002/adma.202100218
10. Zhao, Y.F.; Chen, G.D.; Zhao, Y.Q.; Li, M.; Zhang, N.; Wen, J.; Zhou, N.; Li, S.J.; Mao, H.Y.; Huang, C.J. Wafer-Level, High-Performance, Flexible Sensors Based on Organic Nanoforests for Human–Machine Interactions. *ACS Appl. Mater. Interfaces.* **2023,** *15*, 30793-30803. https://doi.org/10.1021/acsami.3c04953
11. Huo, Y.M.; Bu, M.M.; Ma, Z.T.; Sun, J.Y.; Yan, Y.H.; Xiu, K.H.; Wang, Z.Y.; Hu, N.; Li, Y.F. Flexible, non-contact and multifunctional humidity sensors based on two-dimensional phytic acid doped co-metal organic frameworks nanosheets. *J. Colloid Interface Sci.* **2022,** *607*, 2010-2018. https://doi.org/https://doi.org/10.1016/j.jcis.2021.09.189
12. Shen, L.L.; Feng, W.Q.; Yu, D.; Wang, W. High sensitive humidity sensor based on PEDOT:PSS/CMC-Na coated polyester fabric with directional moisture transport performance. *Colloids Surf., A.* **2024,** *682*, 132880. https://doi.org/https://doi.org/10.1016/j.colsurfa.2023.132880
13. Li, T.K.; Zhao, T.T.; Zhang, H.; Yuan, L.; Cheng, C.C.; Dai, J.S.; Xue, L.W.; Zhou, J.X.; Liu, H.; Yin, L.Q.; Zhang, J.H. A skin-conformal and breathable humidity sensor for emotional mode recognition and non-contact human-machine interface. *npj Flexible Electron.* **2024,** *8*, 3. https://doi.org/10.1038/s41528-023-00290-z
14. Huo, Z.L.; Qiao, J.Y.; Zhang, L.X.; Yue, Y.W.; Qiu, Q.D.; Hou, Z.J.; Yin, J.; Bie, L.J. High-Performance Flexible Humidity Sensors Based on MCl (M = Li, Na, K) Doped PVP/PVDF Self-Supporting Films for Boosted Real-Time Noncontact Moisture Monitoring. *ACS Appl. Polym. Mater.* **2024,** *6*, 7458-7467. https://doi.org/10.1021/acsapm.4c00773
15. Yang, J.H.; Shi, R.L.; Lou, Z.; Chai, R.Q.; Jiang, K.; Shen, G.Z. Flexible Smart Noncontact Control Systems with Ultrasensitive Humidity Sensors. *Small.* **2019,** *15*, 1902801. https://doi.org/https://doi.org/10.1002/smll.201902801
16. Yuan, Z.; Tai, H.L.; Su, Y.J.; Xie, G.Z.; Du, X.S.; Jiang, Y.D. Self-assembled graphene oxide/polyethyleneimine films as high-performance quartz crystal microbalance humidity sensors. *Rare Met.* **2021,** *40*, 1597-1603. https://doi.org/10.1007/s12598-020-01598-9
17. Wu, K.; Guan, X.; Hou, Z.N.; Liu, L.C.; Zhao, H.R.; Liu, S.; Fei, T.; Zhang, T. Humidity sensors based on metal organic frameworks derived polyelectrolyte films. *J. Colloid Interface Sci.* **2021,** *602*, 646-653. https://doi.org/https://doi.org/10.1016/j.jcis.2021.06.064
18. Dong, W.Y.; Ma, Z.H.; Duan, Q. Preparation of stable crosslinked polyelectrolyte and the application for humidity sensing. *Sens. Actuators, B.* **2018,** *272*, 14-20. https://doi.org/https://doi.org/10.1016/j.snb.2018.05.140
19. Dai, J.X.; Zhao, H.R.; Lin, X.Z.; Liu, S.; Fei, T.; Zhang, T. Humidity Sensors Based on 3D Porous Polyelectrolytes via Breath Figure Method. *Adv. Electron. Mater.* **2020,** *6*, 1900846. https://doi.org/https://doi.org/10.1002/aelm.201900846
20. Naguib, M.; Kurtoglu, M.; Presser, V.; Lu, J.; Niu, J.; Heon, M.; Hultman, L.; Gogotsi, Y.; Barsoum, M.W. Two-Dimensional Nanocrystals Produced by Exfoliation of Ti_3AlC_2. *Adv. Mater.* **2011,** *23*, 4248-4253. https://doi.org/https://doi.org/10.1002/adma.201102306
21. Li, J.Y.; Guo, S.J.; Chen, K.L.; Zhao, M.; Wu, W.X.; Xia, X.J.; Zhao, J. CuO nanoparticles embedded in laser-induced graphene for flexible planar micro-supercapacitors. *Surf. Interfaces.* **2024,** *52*, 104968. https://doi.org/https://doi.org/10.1016/j.surfin.2024.104968

22. Mahmood, M.; Rasheed, A.; Ayman, I.; Rasheed, T.; Munir, S.; Ajmal, S.; Agboola, P.O.; Warsi, M.F.; Shahid, M. Synthesis of Ultrathin MnO_2 Nanowire-Intercalated 2D-MXenes for High-Performance Hybrid Supercapacitors. *Energy & Fuels.* **2021,** *35*, 3469-3478. https://doi.org/10.1021/acs.energyfuels.0c03939
23. Sun, J.Y.; Zhao, X.; Illeperuma, W.R.K.; Chaudhuri, O.; Oh, K.H.; Mooney, D.J.; Vlassak, J.J.; Suo, Z. Highly stretchable and tough hydrogels. *Nature.* **2012,** *489*, 133-136. https://doi.org/10.1038/nature11409
24. Yan, B.R.; Hu, X.M.; Zhao, Y.Y.; Wu, M.Y.; Feng, Y.; He, Z.L.; Qi, G.S.; Ren, W.X.; Liang, Y.T.; Wang, W.; Qiao, J.; Zhang, Q. Research and development of a sodium alginate/calcium ion gel based on in situ cross-linked double-network for controlling spontaneous combustion of coal. *Fuel.* **2022,** *322*, 124260. https://doi.org/https://doi.org/10.1016/j.fuel.2022.124260
25. Zhang, Y.Y.; Fan, W.; Huang, Y.P.; Zhang, C.; Liu, T. Graphene/carbon aerogels derived from graphene crosslinked polyimide as electrode materials for supercapacitors. *RSC Adv.* **2015,** *5*, 1301-1308. https://doi.org/10.1039/C4RA13015D
26. Houeix, Y.; Gerardo, D.; Romero, F.J.; Toral, V.; Hernandez, L.; Rivadeneyra, A.; Castillo, E.; Morales, D.P.; Rodriguez, N. Dry Laser-Induced Graphene Fractal-like ECG Electrodes. *Adv. Electron. Mater.* **2024,** *10*, 2300767. https://doi.org/https://doi.org/10.1002/aelm.202300767
27. Zheng, X.R.; Jia, B.H.; Chen, X.; Gu, M. In Situ Third-Order Non-linear Responses During Laser Reduction of Graphene Oxide Thin Films Towards On-Chip Non-linear Photonic Devices. *Adv. Mater.* **2014,** *26*, 2699-2703. https://doi.org/https://doi.org/10.1002/adma.201304681
28. Liu, X.T.; Wu, Z.J.; Jiang, D.W.; Guo, N.; Wang, Y.; Ding, T.; Weng, L. A highly stretchable, sensing durability, transparent, and environmentally stable ion conducting hydrogel strain sensor built by interpenetrating Ca_2^+-SA and glycerol-PVA double physically cross-linked networks. *Adv. Compos. Hybrid Mater.* **2022,** *5*, 1712-1729. https://doi.org/10.1007/s42114-021-00396-w
29. Geng, W.C.; Yuan, Q.; Jiang, X.M.; Tu, J.C.; Duan, L.B.; Gu, J.W.; Zhang, Q.Y. Humidity sensing mechanism of mesoporous MgO/KCl–SiO_2 composites analyzed by complex impedance spectra and bode diagrams. *Sens. Actuators, B.* **2012,** *174*, 513-520. https://doi.org/https://doi.org/10.1016/j.snb.2012.08.057
30. Zhou, C.; Zhang, X.S.; Tang, N.; Fang, Y.; Zhang, H.N.; Duan, X.X. Rapid response flexible humidity sensor for respiration monitoring using nano-confined strategy. *Nanotechnology.* **2020,** *31*, 125302. https://doi.org/10.1088/1361-6528/ab5cda
31. Bao, W.J.; Chen, F.Y.; Lai, H.L.; Liu, S.; Wang, Y.P. Wearable breath monitoring based on a flexible fiber-optic humidity sensor. *Sens. Actuators, B.* **2021,** *349*, 130794. https://doi.org/https://doi.org/10.1016/j.snb.2021.130794
32. Jin, X.F.; Zha, L.; Wang, F.; Wang, Y.Z.; Zhang, X.J. Fully integrated wearable humidity sensor for respiration monitoring. *Front. Bioeng. Biotechnol.* **2022,** *10*, 1070855. https://doi.org/10.3389/fbioe.2022.1070855
33. Zhao, H.J.; Chen, H.Z.; Yang, M.J.; Li, Y. Facile fabrication of poly (diallyldimethyl ammonium chloride)/Ti_3C_2Tx/poly (vinylidene fluoride) 3D hollow fiber membrane flexible humidity sensor and its application in the monitoring of health-related physiological activity. *Sens. Actuators, B.* **2023,** *374*, 132773. https://doi.org/https://doi.org/10.1016/j.snb.2022.132773
34. Li, T.K.; Zhao, T.T.; Tian, X.M.; Yuan, L.; Xue, X.Y.; Wang, Z.G.; Yin, L.Q.; Zhang, J.H. A high-performance humidity sensor based on alkalized MXenes and poly(dopamine) for touchless sensing and respiration monitoring. *J. Mater. Chem. C.* **2022,** *10*, 2281-2289. https://doi.org/10.1039/D1TC05171G
35. Ma, H.L.; Liu, Z.Q.; Lou, J.; Ding, Q.J.; Jiang, Y.F.; Li, X.; Han, W.J. Bacterial cellulose/MWCNT coatings for highly sensitive and flexible paper-based humidity sensors. *Cellulose.* **2023,** *30*, 1193-1204. https://doi.org/10.1007/s10570-022-04960-5